

Waveguiding valley excitons in monolayer transition metal dichalcogenides by dielectric interfaces in the substrate

Xu-Chen Yang ^{1,2}, Hongyi Yu ^{3,*} and Wang Yao ^{1,2}

¹*Department of Physics, The University of Hong Kong, Hong Kong, China*

²*HKU-UCAS Joint Institute of Theoretical and Computational Physics at Hong Kong, Hong Kong, China*

³*Guangdong Provincial Key Laboratory of Quantum Metrology and Sensing and School of Physics and Astronomy, Sun Yat-Sen University, Zhuhai Campus, Zhuhai 519082, China*



(Received 11 October 2021; revised 25 November 2021; accepted 30 November 2021; published 13 December 2021)

In monolayers of semiconducting transition metal dichalcogenides, the electron-hole exchange interaction splits the exciton dispersion into a massive transverse branch and a longitudinal branch that has very light or even zero mass depending on the form of screened Coulomb interaction. The group velocity of the longitudinal branch is sensitive to the strength of electron-hole exchange, which can be engineered through the dielectric environment. Here we show that dielectric patterning of the substrate can be exploited to realize the waveguide of the exciton in the longitudinal branch in a homogeneous monolayer, leaving the massive transverse branch unaffected. At a lateral interface of different dielectric constants in the substrate, the transmission and reflection of the exciton in the longitudinal branch obey the Snell-Descartes law of optical systems, and total reflection can be exploited to realize an excitonic waveguide using two parallel interfaces. The same dielectric pattern of the substrate appears to be completely transparent for the massive transverse branch exciton, which has no interface scattering. When the monolayer is placed on a one-dimensional dielectric superlattice, the dispersion of the longitudinal branch is strongly renormalized, and the wave functions exhibit one-dimensional features, confined to either the low-dielectric or high-dielectric region. In contrast, the massive transverse branch excitons are not affected by the substrate dielectric pattern, exhibiting pristine properties as in a freestanding monolayer.

DOI: [10.1103/PhysRevB.104.245305](https://doi.org/10.1103/PhysRevB.104.245305)

I. INTRODUCTION

Atomically thin group-VIB transition metal dichalcogenides (TMDs) have attracted intensive research interest in the past decade [1–3]. Monolayer TMDs have a covalently bonded two-dimensional (2D) hexagonal lattice, which serves as the elementary unit of layered bulk crystals stacked by a weak van der Waals interaction. In the atomically thin limit, the electronic band structure of the TMDs exhibits direct band gaps in the visible frequency range [4,5], located at the energetically degenerate corners of the hexagonal Brillouin zone. So the conduction and valence band edges both have degeneracies, labeled by the valley indices $\pm\mathbf{K}$. An exciton is a hydrogenlike bound state of the band edge electron and hole created by the Coulomb interaction. The reduced screening of the Coulomb interaction in 2D geometry results in a large binding energy [6–8]. The exciton wave function, on the other hand, is still the Wannier type, with a small Bohr radius on the order of nanometers, well localized in the valleys in momentum space [9]. The valley optical selection rule of the interband transition dictates that an exciton in the \mathbf{K} (or $-\mathbf{K}$) valley interconverts with only a $\sigma+$ (or $\sigma-$) circularly polarized photon [10,11]. Because of the small Bohr radius, the Coulomb exchange interaction between the electron and hole causes a sizable valley-orbit coupling, which splits the exciton

energy-momentum dispersion into two branches of in-plane valley pseudospins, coupled to photons of linear polarization longitudinal and transverse to the exciton momentum [12,13].

The transverse branch has parabolic dispersion with the regular exciton mass (sum of those of the electron and hole). The longitudinal branch either can be massless or can have very light mass depending on the form of the screened Coulomb interaction, and the group velocity is sensitive to the strength of the electron-hole Coulomb exchange, which is inversely proportional to the square of the exciton Bohr radius [12–15]. The latter has implied interesting possibilities to explore the unusual transport properties of excitons, reminiscent of the massless Dirac electron in graphene [16–18].

The Coulomb interaction in the monolayer geometry is notably sensitive to the surrounding environment, i.e., the substrate and the cap layer [19]. Placing monolayer TMDs on different dielectric substrates leads to modulation of the Coulomb interaction strength, which can result in a significant change both in the quasiparticle band gap and in the exciton binding energy [20–26]. Dielectric-dependent band gap renormalization has been exploited to realize lateral heterojunctions in a continuous TMD monolayer placed on a substrate where the two adjacent segments have distinct dielectric constants [27]. For excitons, the effect from modulating the dielectric screening can be subtler. The renormalization in the quasiparticle band gap and that in the exciton binding energy from the dielectric screening by substrate can cancel each other [9,26,28]. The exciton dispersion edge, i.e., energy at

*yuh33@mail.sysu.edu.cn

zero momentum, can be measured as a resonance in the optical spectra. For the $1s$ exciton, experiments have found that this resonance makes a negligible change in different dielectric substrates [23,29–31]. On the other hand, the dielectric screening of the Coulomb interaction can affect the magnitude of the valley-orbit splitting in the exciton dispersion away from the dispersion edge. These finite-momentum exciton states are optically dark, so the effect does not directly manifest in the optical spectral. Nevertheless, the exciton transport properties can be strongly modulated, especially for the longitudinal branch, where the group velocity sensitively responds to the strength of the electron-hole Coulomb exchange [12–15]. This suggests an interesting possibility to tailor exciton properties in monolayer TMDs through patterning a dielectric substrate [27,32–34].

In this work, we show that dielectric patterning of the substrate can be exploited to guide the exciton transport in the longitudinal branch in a homogeneous monolayer while leaving the massive transverse branch unaffected. At a lateral interface where the two adjacent segments of the substrate have distinct dielectric constants, the transmission and reflection of the exciton in the longitudinal branch obey the Snell-Descartes law of optical systems. The critical angle of the total internal reflection is dependent on the ratio of the dielectric constants of the two substrate segments. Using two parallel interfaces, a waveguide can thus be realized for the longitudinal branch exciton. In contrast, such dielectric interfaces of the substrate appear completely transparent for excitons in the transverse branch, which has no interface scattering. When the monolayer is placed on a one-dimensional dielectric superlattice, the dispersion of the longitudinal branch exciton is changed significantly, displaying isotropic and anisotropic energy minima as well as saddle points at the center and edge of the superlattice Brillouin zone. The wave functions can exhibit one-dimensional (1D) features, confined to either the low-dielectric or high-dielectric region. The massive transverse branch excitons are not affected by the substrate dielectric pattern, exhibiting the same 2D parabolic dispersion as in a freestanding monolayer. This creates an interesting hybrid of 1D and 2D excitons in a common homogeneous monolayer.

The rest of this paper is organized as follows. In Sec. II, we introduce the model of monolayer TMD excitons on a periodic patterned dielectric superlattice. Then the miniband dispersions of the excitons are calculated and analyzed in Sec. III. Section IV presents the numerical results for the exciton transmission and reflection at a single lateral interface where the two adjacent segments of the substrate have distinct dielectric constants and puts forward a waveguide design for the massless longitudinal branch exciton using two such interfaces. In Sec. V, we present the spatial features of wave functions showing waveguide confinement of excitons on a dielectric superlattice. Then we discuss the effect of weak energy modulation by the dielectric superlattice in Sec. VI. We summarize in Sec. VII.

II. MODEL

Here we focus on the spin-singlet bright excitons in monolayer TMDs with both the electron and hole constituents

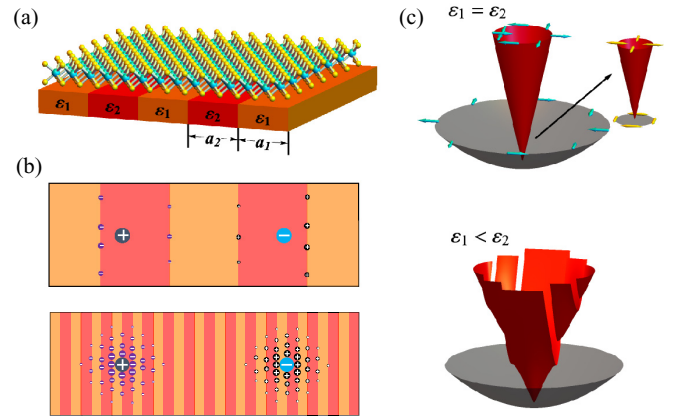


FIG. 1. (a) Schematic diagrams of the monolayer TMDs on a substrate of a quasi-1D patterned dielectric superlattice $\epsilon(\mathbf{R})$ which is along the x direction with period $L = a_1 + a_2$. (b) The Coulomb interaction between the electron (cyan dot) and hole (gray dot) is screened by the surface charges (black and purple dots) emerging at the dielectric interfaces in the long- and short-period limits. (c) Energy dispersion of the exciton in a homogeneous dielectric environment (top) and in a dielectric superlattice $\epsilon(\mathbf{R})$ (bottom), where red (gray) stands for the L (T) branch. The cyan single-headed arrows denote the valley pseudospin of excitons. In the inset of the dispersion in the light cone, the yellow double-headed arrows denote the linear polarization of the emitted photon on exciton recombination.

located in the $+\mathbf{K}$ or $-\mathbf{K}$ valley. Meanwhile, the spins of the electron and hole are opposite, so the excitonic valley index is locked with its real spin ($+\mathbf{K}$ or $-\mathbf{K}$, corresponding to \uparrow or \downarrow) due to the large spin-orbit splitting from the transition metal atom. The Coulomb exchange interaction between the electron and hole leads to the coupling between the two valleys, which breaks the valley degeneracy at finite center-of-mass (c.m.) momenta. The exchange splitting depends sensitively on the Coulomb interaction, which can be modulated spatially by placing the monolayer TMDs on a substrate with a patterned dielectric superlattice, schematically shown in Fig. 1(a). A general form of the Coulomb interaction can be written as $V(\mathbf{R}, \mathbf{r}_{eh}) = \frac{e^2}{\epsilon(\mathbf{R}, \mathbf{r}_{eh})r_{eh}}$, with $\epsilon(\mathbf{R}, \mathbf{r}_{eh})$ being the effective dielectric screening experienced by the electron-hole pair, which depends on the electron-hole separation (relative coordinate) $\mathbf{r}_{eh} \equiv \mathbf{r}_e - \mathbf{r}_h$ [35] and now also spatially varies with the c.m. coordinate $\mathbf{R} \equiv \frac{m_e}{M_0}\mathbf{r}_e + \frac{m_h}{M_0}\mathbf{r}_h$ due to the patterned dielectric. $\mathbf{r}_{e/h}$ denotes the electron or hole spatial coordinate.

In the valley pseudospin space, the exchange interaction can be written as

$$\hat{H}_{ex} = \sum_{\mathbf{k}, \mathbf{k}', \tau, \tau'} J_{\tau\tau'}(\mathbf{k}, \mathbf{k}') \hat{B}_{\mathbf{k}, \tau}^\dagger \hat{B}_{\mathbf{k}', \tau'}. \quad (1)$$

Here $\hat{B}_{\mathbf{k}, \tau}^\dagger$ ($\hat{B}_{\mathbf{k}, \tau}$) creates (annihilates) an exciton with the c.m. momentum $\mathbf{k} = (k_x, k_y) = (k \cos \theta, k \sin \theta)$ and the valley pseudospin $\tau = +, -$, which can be described by the wave function $X_{\mathbf{k}, \tau}(\mathbf{r}_e, \mathbf{r}_h) \equiv \sum_{\mathbf{q}} \Phi(\mathbf{q}) \psi_{\mathbf{q} + \frac{m_e}{M_0}\mathbf{k}, \tau}(\mathbf{r}_e) \psi_{\mathbf{q} - \frac{m_h}{M_0}\mathbf{k}, \tau}^*(\mathbf{r}_h)$. $\psi_{\mathbf{k}, c/v, \tau}(\mathbf{r}_{e/h})$ is the conduction or valence band Bloch state at a wave vector away from $\tau\mathbf{K}$ by \mathbf{k} . The exciton mass $M_0 = m_e + m_h \approx 0.7m_0$,

with $m_e \approx m_h$ and m_0 being the free-electron mass. $J_{+/-/+}$ ($J_{++/--}$) is the strength of the intervalley (intravalley) Coulomb exchange interaction whose amplitude is (see Appendix A for details)

$$J_{\tau,\tau'}(\mathbf{k}, \mathbf{k}') = \int d\mathbf{r}_e d\mathbf{r}_h X_{\mathbf{k},\tau}^*(\mathbf{r}_e, \mathbf{r}_e) V(\mathbf{R}, \mathbf{r}_{eh}) X_{\mathbf{k}',\tau'}(\mathbf{r}_h, \mathbf{r}_h) \\ = (\mathbf{k} \cdot \mathbf{d}_{X,\tau})(\mathbf{k}' \cdot \mathbf{d}_{X,\tau}') V\left(\mathbf{k} - \mathbf{k}', \frac{m_e}{M_0} \mathbf{k} + \frac{m_e}{M_0} \mathbf{k}'\right). \quad (2)$$

In the above equation we have dropped the short-range part of the exchange interaction, as it depends weakly on the momenta and thus can be viewed as a constant for small values of k and k' (see Appendix A for details). $\mathbf{d}_{X,\tau}$ is the optical dipole of the exciton, and

$$V(\mathbf{Q}, \mathbf{k}) \equiv \int d\mathbf{r}_{eh} d\mathbf{R} e^{-i\mathbf{k} \cdot \mathbf{r}_{eh}} e^{-i\mathbf{Q} \cdot \mathbf{R}} V(\mathbf{R}, \mathbf{r}_{eh}). \quad (3)$$

As the Coulomb interaction $V(\mathbf{R}, \mathbf{r}_{eh})$ now varies with the c.m. coordinate \mathbf{R} , generally, $J_{\tau,\tau'}(\mathbf{k}, \mathbf{k}') \neq 0$ for $\mathbf{k} \neq \mathbf{k}'$.

In monolayer TMDs, the valley optical selection rule indicates that the exciton in the $+\mathbf{K}$ (or $-\mathbf{K}$) valley can interconvert only with a $\sigma+$ (or $\sigma-$) circularly polarized photon. Such a circularly polarized selection rule originates from the $2\pi/3$ rotational symmetry of the lattice and is expected to hold as long as the length scale of the spatial modulation of the dielectric constant is much larger than the monolayer lattice constant. So the optical dipole of the $\tau\mathbf{K}$ valley exciton is $\mathbf{d}_{X,\tau} \equiv (d_{X,\tau}^x, d_{X,\tau}^y) = \frac{D}{\sqrt{2}}(i\tau, 1)$ [12], and

$$J_{\tau,\tau'}(\mathbf{k}, \mathbf{k}') = \frac{D^2}{2} k k' (e^{-i\tau\theta} + e^{i\tau'\theta'}) V\left(\mathbf{k} - \mathbf{k}', \frac{m_e}{M_0} \mathbf{k} + \frac{m_e}{M_0} \mathbf{k}'\right). \quad (4)$$

The exchange Hamiltonian then becomes

$$\hat{H}_{ex} = D^2 \sum_{\mathbf{k}, \mathbf{k}'} k k' V\left(\mathbf{k} - \mathbf{k}', \frac{m_e}{M_0} \mathbf{k} + \frac{m_e}{M_0} \mathbf{k}'\right) \hat{B}_{\mathbf{k},L}^\dagger \hat{B}_{\mathbf{k}',L}. \quad (5)$$

Here $\hat{B}_{\mathbf{k},L}^\dagger \equiv \frac{1}{\sqrt{2}}(e^{-i\theta_{\mathbf{k}}} \hat{B}_{\mathbf{k},+}^\dagger + e^{i\theta_{\mathbf{k}}} \hat{B}_{\mathbf{k},-}^\dagger)$ and $\hat{B}_{\mathbf{k},T}^\dagger \equiv \frac{1}{\sqrt{2}}(e^{-i\theta_{\mathbf{k}}} \hat{B}_{\mathbf{k},+}^\dagger - e^{i\theta_{\mathbf{k}}} \hat{B}_{\mathbf{k},-}^\dagger)$ are the creation operators of the longitudinal (L) and transverse (T) branches, respectively, which emit linearly polarized photons with polarization angles longitudinal and transverse to the direction of \mathbf{k} .

Interestingly, due to the circularly polarized valley optical selection rule the Coulomb exchange interaction affects only the L branch, while the T branch is totally unaffected. Note that this conclusion is independent of the form of the Coulomb interaction $V(\mathbf{R}, \mathbf{r}_{eh})$.

Below, we consider one-dimensional modulation of the dielectric; that is, the local dielectric constant $\varepsilon(\mathbf{R}) \equiv \varepsilon(\mathbf{R}, \mathbf{r}_{eh} \rightarrow 0)$ periodically varies in only the x direction. In the period $x \in [-L/2, L/2]$,

$$\varepsilon(\mathbf{R}) = \begin{cases} \varepsilon_1 = \varepsilon_0, & -a_1/2 \leq x < a_1/2, \\ \varepsilon_2 = \xi_\varepsilon \cdot \varepsilon_1, & \text{otherwise,} \end{cases} \quad (6)$$

which is schematically shown in Fig. 1(a). We emphasize that for an electron-hole pair separated by $\mathbf{r}_{eh} \neq 0$, the effective dielectric screening $\varepsilon(\mathbf{R}, \mathbf{r}_{eh})$ of their Coulomb interaction can be different from the local value $\varepsilon(\mathbf{R})$. Nevertheless, the

dielectric constant $\varepsilon(\mathbf{R}, \mathbf{r}_{eh})$ always has the same periodicity as a function of the c.m. coordinate \mathbf{R} , so $V(\mathbf{Q}, \mathbf{k}) = \sum_{\mathbf{g}} \delta_{\mathbf{Q},\mathbf{g}} V(\mathbf{g}, \mathbf{k})$, where \mathbf{g} is the reciprocal lattice vector of the dielectric superlattice.

III. RENORMALIZATION OF THE EXCITON DISPERSION BY THE PATTERNED DIELECTRIC SUPERLATTICE

The energy dispersion of the monolayer exciton is determined by the total Hamiltonian

$$\hat{H} = \hat{H}_{\mathbf{k}} + \hat{H}_{ex} = \sum_{\mathbf{k}} \frac{\hbar^2 k^2}{2M_0} (\hat{B}_{\mathbf{k},L}^\dagger \hat{B}_{\mathbf{k},L} + \hat{B}_{\mathbf{k},T}^\dagger \hat{B}_{\mathbf{k},T}) \\ + D^2 \sum_{\mathbf{k}, \mathbf{k}'} k k' V\left(\mathbf{k} - \mathbf{k}', \frac{m_e}{M_0} \mathbf{k} + \frac{m_e}{M_0} \mathbf{k}'\right) \hat{B}_{\mathbf{k},L}^\dagger \hat{B}_{\mathbf{k}',L}. \quad (7)$$

The Hamiltonian indicates that the dispersion of the L branch is modulated by the patterned dielectric substrate, while the dispersion of the T branch remains unchanged.

In the case of a homogeneous dielectric substrate $\varepsilon_2 = \varepsilon_1$ (i.e., $\xi_\varepsilon = 1$), the Coulomb potential $V(\mathbf{R}, \mathbf{r}_{eh}) = V(\mathbf{r}_{eh})$ depends on only \mathbf{r}_{eh} , and $V(\mathbf{Q}, \mathbf{k}) = \delta_{\mathbf{Q},0} V(\mathbf{k})$, with $V(\mathbf{k}) \equiv \int d\mathbf{r}_{eh} e^{-i\mathbf{k} \cdot \mathbf{r}_{eh}} V(\mathbf{r}_{eh}) = \frac{2\pi e^2}{\varepsilon_0(k+k_s)}$ when taking into account the screening effect from free carriers. The resultant exchange interaction couples only two excitons with the same c.m. momentum,

$$\hat{H}_{ex} = \frac{2\pi e^2 D^2}{\varepsilon_0} \sum_{\mathbf{k}} \frac{k^2}{k+k_s} \hat{B}_{\mathbf{k},L}^\dagger \hat{B}_{\mathbf{k},L}. \quad (8)$$

The result illustrates that the exciton's energy band is split into two branches of in-plane valley pseudospins, coupled to photons with linear polarization longitudinal and transverse to the exciton momentum [12,13]. The T branch has a parabolic dispersion with the regular exciton mass, while the L branch either can be massless or can have a very light mass, depending on the screening wave vector k_s . In the limit of low free-carrier density, the screening wave vector $k_s = \frac{2m^* e^2}{\varepsilon_0 \hbar^2} f_0$, where f_0 is the Fermi-Dirac distribution of the electron or hole at the $\pm\mathbf{K}$ point. For $k_s = 0$ the L branch has a linear dispersion near $\mathbf{k} = 0$. The dispersion of the exciton is shown in the top panel of Fig. 1(c).

For an inhomogeneous dielectric superlattice with $\varepsilon_2 \neq \varepsilon_1$, we can expand the effective dielectric constant into the Fourier series $\varepsilon^{-1}(\mathbf{R}, \mathbf{r}_{eh}) = \varepsilon_0^{-1} \sum_{\mathbf{g}} \alpha(\mathbf{g}, \mathbf{r}_{eh}) e^{i\mathbf{g} \cdot \mathbf{R}}$. In this case $V(\mathbf{g}, \mathbf{k}) = \frac{e^2}{\varepsilon_0} \int d\mathbf{r}_{eh} \alpha(\mathbf{g}, \mathbf{r}_{eh}) \frac{e^{-i\mathbf{k} \cdot \mathbf{r}_{eh}}}{r_{eh}}$ is generally nonzero for $\mathbf{g} \neq 0$. Note that surface charges can appear at the dielectric interface between ε_1 and ε_2 , which can effectively screen the Coulomb interaction between the electron and hole, as schematically shown in Fig. 1(b). Such a mechanism is analogous to the effect from the free carriers; thus, we write the Coulomb interaction form as $V(\mathbf{g}, \mathbf{k}) = \alpha(\mathbf{g}) \frac{2\pi e^2}{\varepsilon_0} \frac{1}{k_0(\mathbf{g})+k}$, with $\alpha(\mathbf{g}) \equiv \alpha(\mathbf{g}, \mathbf{r}_{eh} = 0)$. $k_0(\mathbf{g})$ is the screening wave vector from the surface charges, which is a function of the modulation period L or the reciprocal lattice vector \mathbf{g} . In the long-period limit ($L \rightarrow \infty$) the Coulomb interaction becomes the unscreened form, i.e., $k_0(\mathbf{g} = 0) = 0$. Furthermore, the surface charges appear only at the dielectric interface; thus, there are more charges for a smaller L where the screening

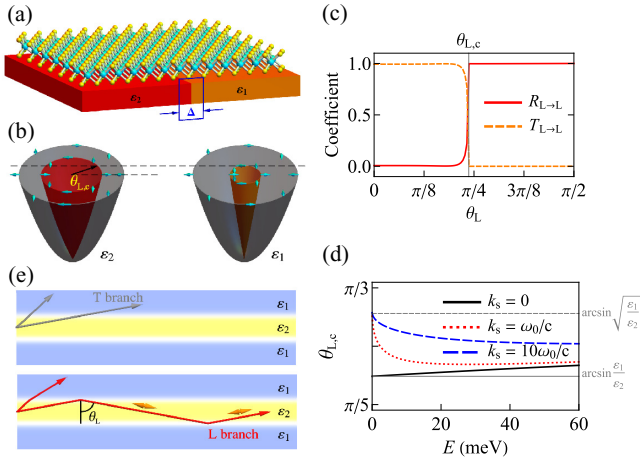


FIG. 2. (a) Schematic diagrams of the monolayer TMDs at a lateral interface, where the two adjacent regions have distinct dielectric constants (ϵ_1 and ϵ_2). A transitional zone with widths Δ is at the interface. (b) Energy dispersion and valley pseudospin of the excitons in each region. The critical angle $\theta_{L,c}$ of the total internal reflection is marked. (c) Transmission and reflection of the L branch incidence as a function of incident angle θ_L in $k_s = 0$. (d) $\theta_{L,c}$ as a function of the exciton energy E . For the black solid, red dotted, and blue dashed lines, the screening wave vector $k_s = 0, 1, \text{ and } 10$, respectively, in units of ω_0/c . The limit value of $\theta_{L,c}$ is shown by a dashed gray line for $\arcsin(\epsilon_1/\epsilon_2)$ and a solid gray line for $\arcsin\sqrt{\epsilon_1/\epsilon_2}$. (e) Schematic diagrams of an excitonic waveguide formed by three dielectric regions (ϵ_1 - ϵ_2 - ϵ_1). The propagating directions of the L (T) branch are denoted by red (gray) single-headed arrows. The yellow double-headed arrows denote the linear polarization of the coupled photons. Parameters: $\Delta = 20$ nm, $J = 2$ eV, and $\xi_\epsilon = 1.5$.

becomes more efficient, implying that $k_0(\mathbf{g})$ increases with g . Accordingly, we adopt the form $k_0(\mathbf{g}) = \lambda g$, with λ being a tunable parameter; then the Coulomb exchange interaction is

$$\hat{H}_{\text{ex}} = \frac{J}{K} \sum_{\mathbf{k}, \mathbf{k}'} \delta_{\mathbf{k}', \mathbf{k} + \mathbf{g}} \alpha(\mathbf{g}) \frac{k k'}{\lambda g + \left| \frac{m_b}{M_0} \mathbf{k} + \frac{m_c}{M_0} \mathbf{k}' \right|} \hat{B}_{\mathbf{k}, L}^\dagger \hat{B}_{\mathbf{k}', L}, \quad (9)$$

with $J \equiv \frac{2\pi e^2 D^2}{\epsilon_0} K \sim 2$ eV (see Appendix A for details). The dispersion of the exciton is shown in the bottom panel of Fig. 1(c).

IV. SCATTERING ANALYSIS AT A LATERAL INTERFACE

Here we first analyze the scattering of the exciton in a monolayer at a lateral interface, where the two adjacent regions of the substrate (labeled by $\eta = 1, 2$) have distinct dielectric constants ϵ_η [Fig. 2(a)]. In region η , the Hamiltonian of the exciton can be written as [13]

$$\hat{H}_\eta = \frac{\hbar^2 k^2}{2M_0} + J_{\mathbf{k}, \eta}^{\text{intra}} + [J_{\mathbf{k}, \eta}^{\text{inter}} \hat{\sigma}_+ + \text{H.c.}], \quad (10)$$

where the valley pseudospin raising and lower operators $\hat{\sigma}_\pm = (\hat{\sigma}_x \pm i\hat{\sigma}_y)/2$. The intervalley coupling is $J_{\mathbf{k}, \eta}^{\text{inter}} = \frac{\pi e^2 D^2}{\epsilon_\eta(k+k_s)} k^2 e^{-2i\theta}$ and intravalley coupling is $J_{\mathbf{k}, \eta}^{\text{intra}} = |J_{\mathbf{k}, \eta}^{\text{inter}}|$. \hat{H}_η splits the exciton into the L and T branches. The eigenstates can be written as the direct product of the orbital and valley pseudospin parts $|\psi_{\eta, \chi}(\mathbf{r})\rangle = |\phi_\eta(\mathbf{r})\rangle \otimes |\chi\rangle$, $\chi = L, T$.

Figure 2(b) shows the energy dispersion and valley pseudospin of the exciton in the two regions.

While the interface can be sharp in the substrate, there can be a finite length scale for the variation of the local dielectric constant experienced by the exciton in the monolayer, given the finite vertical distance and the exciton radius. Therefore, we considered a Δ -width transitional region where the local dielectric constant changes continuously from the value of the left region to the value of the right region. In the scattering analysis, this transitional region is divided into n equal pieces with the local dielectric constant $[i\epsilon_1 + (n-i)\epsilon_2]/n$ at the i th piece, and the wave functions are matched with the boundary conditions [Eq. (C3) in Appendix C]. The exciton state in each region can be written as $|\Psi_\eta(\mathbf{r})\rangle = \sum_{\chi=L, T} c_{\eta, \chi} |\psi_{\eta, \chi}(\mathbf{r})\rangle$, where the coefficients $c_{\eta, \chi}$ are determined by boundary conditions (see Appendix C for details). With the translational invariance in the y direction, k_y is a good quantum number. The number of steps n is increased until the results saturate, such that the scattering by a smooth transition of the dielectric constant over the length scale Δ is obtained. The x -component current density of the χ branch exciton is $j_{\eta, \chi}^x = |c_{\eta, \chi}|^2 \langle \psi_{\eta, \chi}(\mathbf{r}) | \hat{v}_{\eta, x} | \psi_{\eta, \chi}(\mathbf{r}) \rangle$, where the velocity operator is $\hat{v}_{\eta, x} = [x, \hat{H}_\eta]/i\hbar$ [36]. The coefficient $R_{\chi \rightarrow \chi'}$ ($T_{\chi \rightarrow \chi'}$) is defined as the ratio between the reflection (transmission) current of the χ' branch and the incident current of the χ branch.

Our calculation finds that the T branch exciton is not affected by the dielectric lateral interface, i.e., $T_{T \rightarrow T} = 1$ and $R_{T \rightarrow T} = 0$, consistent with the fact that the T branch dispersion is unchanged across the dielectric interface. Moreover, scattering between the T and L branches is insignificant. The L branch is significantly affected. $T_{L \rightarrow L}$ and $R_{L \rightarrow L}$ are shown in Fig. 2(c) as functions of the incident angle θ_L in the unscreened limit ($k_s = 0$). $T_{L \rightarrow L}$ is close to unity for a large range of incident angle around the normal incidence. When θ_L is above a critical angle $\theta_{L,c}$, $T_{L \rightarrow L}$ suddenly drops to zero, while $R_{L \rightarrow L}$ rises quickly to unity, becoming the dominant outgoing channel. This phenomenon is similar to the phenomenon of light passing through an interface with different media in an optical system. The incident angle θ_L and the refraction angle ϕ_L obey the Snell-Descartes law,

$$k_L \sin \theta_L = q_L \sin \phi_L, \quad (11)$$

where the wave vectors of the L branch excitons in the two adjacent regions are k_L and q_L (a detail expression is given in Appendix C). The critical angle $\theta_{L,c}$ depends on k_s and exciton scattering energy E , as shown in Fig. 2(d). In the low-energy limit, $\theta_{L,c} \approx \arcsin(\epsilon_1/\epsilon_2)$ at $k_s = 0$, while $\theta_{L,c} \approx \arcsin\sqrt{\epsilon_1/\epsilon_2}$ at $k_s = 10\omega_0/c$. The parameters adopted in the calculation are $\Delta = 20$ nm, $J = 2$ eV, $\hbar\omega_0 = 2$ meV, and $\xi_\epsilon = 1.5$.

The photonlike scattering behavior suggests that an excitonic waveguide can be realized for the L branch excitons by patterning the substrate dielectric as $\epsilon_1 - \epsilon_2 - \epsilon_1$ ($\epsilon_1 < \epsilon_2$) with two parallel interfaces, as schematically shown in Fig. 2(d). We consider an exciton wave packet in region ϵ_2 , whose angle of the propagating direction is θ_L . While the T branch exciton is always transmitted through the interface, the transmission or reflection of the L branch is determined by the angle θ_L . When $\theta_L > \theta_{L,c}$, the L branch exciton has total

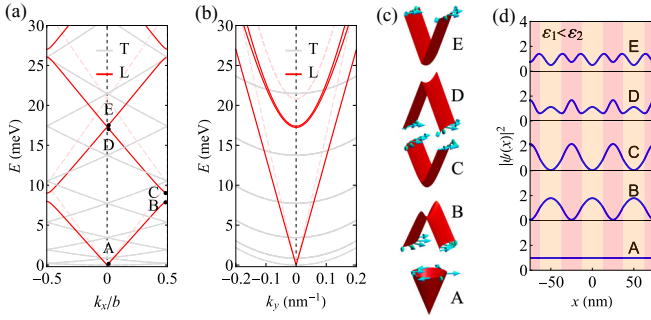


FIG. 3. Renormalized energy dispersion of the exciton in a 1D dielectric superlattice $\varepsilon(\mathbf{R})$, where the red (gray) solid lines stand for the L (T) branch. Dispersion in the homogeneous dielectric environment is denoted by the dashed lines. (a) Dispersion as a function of k_x at $k_y = 0$. (b) Dispersion as a function of k_y at $k_x = 0$. (c) Dispersions and valley pseudospin of the L branch exciton near the centers (A, D, E) and edges (B, C) of the superlattice Brillouin zone. (d) One-dimensional features of the L branch exciton's wave function. Parameters: $J = 2$ eV, $\xi_\varepsilon = 1.5$, and $a_1 = a_2 = 25$ nm.

reflection at the interface. Otherwise ($\theta_L < \theta_{L,c}$), it refracts outside. Thus, the L branch with small θ_L is confined in dielectric region ε_2 , and an excitonic waveguide is achieved.

The exciton with large kinetic energy is located outside the light cone and thus has a long lifetime, which facilitates its propagation in the waveguide. Its radiative recombination can be assisted by the scattering with a phonon into the light cone followed by photon emission. As schematically shown in Figs. 2(b) and 2(e), because of the valley-momentum locking in the L branch, the exciton confined in dielectric region ε_2 has an in-plane valley pseudospin locked in the propagation direction, and therefore, through the valley optical selection rule, photon emission is expected with linear polarization correlated with the waveguide orientation. On the other hand, we note that the waveguide defined by these parallel dielectric interfaces can play the role of transport channels. Hot excitons created by the above-resonance excitation can be guided, with low radiative loss, towards designated regions, where excitons can relax their kinetic energy for efficient emission. This points to new possibilities to design exciton-based optoelectronic devices.

V. WAVEGUIDE CONFINEMENT OF THE EXCITON'S WAVE FUNCTION

The scattering analysis in the previous section suggests waveguide confinement of the exciton by two adjacent dielectric interfaces. Here we further examine this 1D propagation of the L branch excitons by solving the exciton wave function in a 1D dielectric superlattice consisting of periodically arranged parallel interfaces, where the dielectric coefficient $\varepsilon(\mathbf{R})$ is described by Eq. (6), as shown in Fig. 1(a), with $a_1 = a_2 = 25$ nm, $\varepsilon_2 = 1.5\varepsilon_1$, and $\lambda = 1$.

The renormalized energy dispersion of the exciton along the x axis ($k_y = 0$) is shown in Fig. 3(a). While the T branch (gray solid lines) is not affected by the substrate dielectric pattern, the dispersion of the L branch exciton (red solid lines) is changed significantly. For the lowest band near $\mathbf{k} = 0$, the L branch remains linear but has a renormalized group velocity,

compared to the homogeneous dielectric case (red dashed lines), and the reduced group velocity is proportional to ξ_ε . Furthermore, band gap opens for the L branch at the center or edge of the superlattice Brillouin zone. Figure 3(b) shows the dispersion along the y axis and $k_x = 0$. Figure 3(c) is an enlarged view of dispersions of the exciton L branch near the center (A, D, E) and edges (B, C) of the superlattice Brillouin zone. The L branch has isotropic energy minima and isotropic group velocity near A but is anisotropic near C or B. For instance, saddle shapes of energy minima appear at the B and D points.

The patterned dielectric superlattice also introduces 1D modulations to the exciton's wave function. Figure 3(a) shows the density distributions of the L branch at momentum-space positions A to E. At the lowest-energy A point, the exciton density remains constant in real space due to the fact that the exchange matrix element $J_{\tau,\tau'}(\mathbf{k}, \mathbf{k}') = 0$ when $kk' = 0$. However, the densities at other higher-energy positions exhibit spatial modulations, confined to either the low-dielectric or high-dielectric regions. For instance, the calculated density distributions indicate that the low-energy mode at B has dominant probability in the low- ε regions, while the high-energy mode at C concentrates in the high- ε regions. A similar phenomenon is presented between the second band (D point) and the third band (E point) of the L exciton branch at the center of the superlattice Brillouin zone $k = 0$. These spatial features are not sensitive to the smooth interface length Δ or the screening wave vector parameter λ .

VI. EFFECTS OF ENERGY MODULATION IN THE DIELECTRIC SUPERLATTICE

In the above analysis, we assumed that the exciton energy remains constant when we modulate the dielectric environment, as the resultant changes to the exciton binding energy and electronic band gap almost cancel each other for the 1s exciton [9,26,28]. In realistic systems this cancellation is not exact, and there can be a modest modulation ΔV in the energy of both exciton branches, as shown in Fig. 4(a). We examine the effect of this energy modulation on the scattering result at a lateral interface (in Sec. IV) in the unscreened limit $k_s = 0$. We adopt the condition that ΔV has a modulation amplitude of 5 meV. Figure 4(c) shows $R_{T \rightarrow T}$ and $T_{T \rightarrow T}$ as functions of the incident angle θ_T . The results show that the T branch exciton is now affected by the interface as well. $T_{T \rightarrow T} = 1$ for incident angles around the normal incidence. When θ_T is above a critical angle $\theta_{T,c}$, the total internal reflection occurs, $R_{T \rightarrow T} = 1$ and $T_{T \rightarrow T} = 0$. For the L branch, the total internal reflection still exists at the interface [in Fig. 4(b)] with the critical angle $\theta_{L,c}$ depending on ΔV and the exciton energy E . Figure 4(d) shows the critical angles $\theta_{L,c}$ and $\theta_{T,c}$ as a function of E .

In the case of excitons on the 1D dielectric superlattice (in Sec. V), these spatial features of the L branch exciton's wave functions are not sensitive to low-energy modulation (i.e., amplitude of ΔV less than 4 meV) coming from the spatially varying dielectric constant (see Appendix D for details).

VII. SUMMARY

In summary, we have put forward a design of an excitonic waveguide for the longitudinal branch by placing a

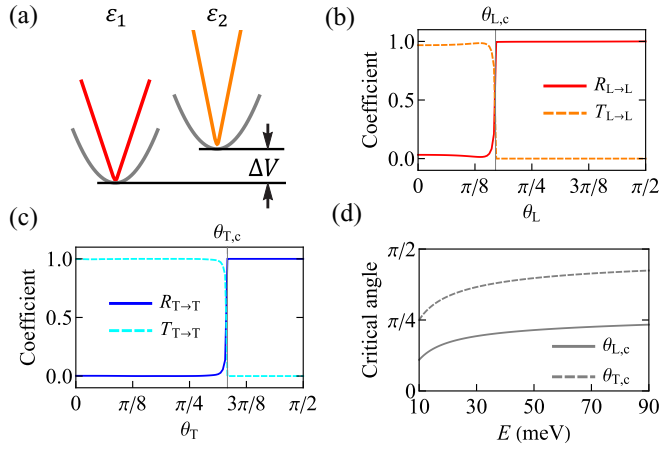


FIG. 4. Effect of the energy modulation coming from the spatially varying dielectric constant. (a) Energy modulation ΔV_0 . For (b) the L branch incidence and (c) the T branch incidence, the transmission and reflection as a function of incident angle. The total internal reflection occurs at critical angles $\theta_{L,c}$ and $\theta_{T,c}$, respectively. (d) The critical angle as a function of the exciton energy E . Parameters: ΔV with an amplitude of 5 meV, $E = 20$ meV for (b) and (c), $J = 2$ eV, $k_s = 0$, and $\xi_s = 1.5$.

homogeneous monolayer TMDs on a patterned dielectric substrate, which does not affect the massive transverse branch. In a lateral dielectric interface, the L branch exciton's transmission and reflection satisfy the Snell-Descartes law of optical systems. Nevertheless, this dielectric heterostructure appears to be transparent to the transverse branch. Placing the monolayer on a 1D periodic dielectric superlattice, we find that the longitudinal branch excitons have strongly renormalized dispersion and 1D spatially featured wave functions. In contrast,

the transverse branch excitons are not affected by the substrate dielectric pattern.

ACKNOWLEDGMENTS

The work is supported by the University Grants Committee/Research Grant Council of the Hong Kong SAR (Grant No. AoE/P-701/20), a Croucher Senior Research Fellowship, and HKU Seed Funding for Strategic Interdisciplinary Research. H.Y. acknowledges support from the Department of Science and Technology of Guangdong Province in China (Grant No. 2019QN01X061).

APPENDIX A: MODEL OF THE MONOLAYER TMD EXCITON IN A PERIODIC DIELECTRIC SUPERLATTICE

We consider two bright excitons, $\hat{B}_{\mathbf{k},+}^\dagger$ and $\hat{B}_{\mathbf{k},-}^\dagger$, which correspond to states in opposite valleys with opposite spins,

$$\begin{aligned} X_{\mathbf{k},+}(\mathbf{r}_e, \mathbf{r}_h) &= \sum_{\mathbf{q}} \Phi^*(\mathbf{q}) \psi_{\mathbf{q}+\frac{m_e}{M_0}\mathbf{k},c,+}(\mathbf{r}_e) \psi_{\mathbf{q}-\frac{m_h}{M_0}\mathbf{k},v,+}^*(\mathbf{r}_h), \\ X_{\mathbf{k},-}(\mathbf{r}_e, \mathbf{r}_h) &= \sum_{\mathbf{q}} \Phi(-\mathbf{q}) \psi_{\mathbf{q}+\frac{m_e}{M_0}\mathbf{k},c,-}(\mathbf{r}_e) \psi_{\mathbf{q}-\frac{m_h}{M_0}\mathbf{k},v,-}^*(\mathbf{r}_h), \end{aligned} \quad (\text{A1})$$

where the c.m. momentum $\mathbf{k} = (k_x, k_y) = (k \cos \theta, k \sin \theta)$ and the valley pseudospin $\tau = +, -$. $\psi_{\mathbf{q},c/v,\tau}(\mathbf{r}_{e/h})$ are the conduction and valence band Bloch states at a wave vector away from $\tau\mathbf{K}$ by \mathbf{q} , and $\Phi(\mathbf{q})$ is the wave function of the relative motion between the electron and hole. The intervalley Coulomb exchange couples the two different valleys, $\hat{H}_{\text{ex,inter}} = J_{+-}(\mathbf{k}, \mathbf{k}') \hat{B}_{\mathbf{k},+}^\dagger \hat{B}_{\mathbf{k}',-}^\dagger + \text{H.c.}$, while the intravalley Coulomb exchange couples the same valley, $\hat{H}_{\text{ex,intra}} = \sum_{\tau} J_{\tau\tau}(\mathbf{k}, \mathbf{k}') \hat{B}_{\mathbf{k},\tau}^\dagger \hat{B}_{\mathbf{k}',\tau}^\dagger$.

The intervalley matrix element is

$$J_{+-}(\mathbf{k}, \mathbf{k}') = \int d\mathbf{r}_e d\mathbf{r}_h \left[\sum_{\mathbf{q}} \Phi(\mathbf{q}) \psi_{\mathbf{q}+\frac{m_e}{M_0}\mathbf{k},c,+}^*(\mathbf{r}_e) \psi_{\mathbf{q}-\frac{m_h}{M_0}\mathbf{k},v,+}(\mathbf{r}_e) \right] V(\mathbf{R}, \mathbf{r}_{eh}) \left[\sum_{\mathbf{q}'} \Phi(-\mathbf{q}') \psi_{\mathbf{q}'+\frac{m_e}{M_0}\mathbf{k}',c,-}(\mathbf{r}_h) \psi_{\mathbf{q}'-\frac{m_h}{M_0}\mathbf{k}',v,-}^*(\mathbf{r}_h) \right]. \quad (\text{A2})$$

Here $V(\mathbf{R}, \mathbf{r}_{eh})$ is the Coulomb potential, which depends on both the relative coordinate \mathbf{r}_{eh} and the center-of-mass coordinate \mathbf{R} due to the spatially varying dielectric constant $\varepsilon(\mathbf{R})$. The Bloch wave functions

$$\begin{aligned} \psi_{\mathbf{q},c(v),+}(\mathbf{r}_e) &= e^{i(\mathbf{K}+\mathbf{q})\cdot\mathbf{r}_e} u_{\mathbf{q},c(v),+}(\mathbf{r}_e) = e^{i(\mathbf{K}+\mathbf{q})\cdot\mathbf{r}_e} \sum_{\mathbf{G}} C_{\mathbf{q},c(v),+}(\mathbf{G}) e^{i\mathbf{G}\cdot\mathbf{r}_e}, \\ \psi_{\mathbf{q},c(v),-}(\mathbf{r}_h) &= e^{i(-\mathbf{K}+\mathbf{q})\cdot\mathbf{r}_h} u_{\mathbf{q},c(v),-}(\mathbf{r}_h) = e^{i(-\mathbf{K}+\mathbf{q})\cdot\mathbf{r}_h} \sum_{\mathbf{G}} C_{\mathbf{q},c(v),-}(\mathbf{G}) e^{i\mathbf{G}\cdot\mathbf{r}_h}. \end{aligned} \quad (\text{A3})$$

The matrix element can be written as $J_{+-}(\mathbf{k}, \mathbf{k}') = \sum_{\mathbf{q}\mathbf{q}'} \Phi(\mathbf{q}) \Phi(-\mathbf{q}') J_{+-}(\mathbf{q}, \mathbf{q}', \mathbf{k}, \mathbf{k}')$, with

$$\begin{aligned} J_{+-}(\mathbf{q}, \mathbf{q}', \mathbf{k}, \mathbf{k}') &= \int d\mathbf{r}_e d\mathbf{r}_h e^{i(\mathbf{k}'\cdot\mathbf{r}_h - \mathbf{k}\cdot\mathbf{r}_e)} u_{\mathbf{q}+\frac{m_e}{M_0}\mathbf{k},c,+}^*(\mathbf{r}_e) u_{\mathbf{q}-\frac{m_h}{M_0}\mathbf{k},v,+}(\mathbf{r}_e) V(\mathbf{R}, \mathbf{r}_e - \mathbf{r}_h) u_{\mathbf{q}'+\frac{m_e}{M_0}\mathbf{k}',c,-}(\mathbf{r}_h) u_{\mathbf{q}'-\frac{m_h}{M_0}\mathbf{k}',v,-}^*(\mathbf{r}_h) \\ &= \sum_{\mathbf{G}, \Delta\mathbf{G}, \mathbf{G}', \Delta\mathbf{G}'} C_{\mathbf{q}+\frac{m_e}{M_0}\mathbf{k},c,+}^*(\mathbf{G}) C_{\mathbf{q}-\frac{m_h}{M_0}\mathbf{k},v,+}(\mathbf{G} + \Delta\mathbf{G}) C_{\mathbf{q}'+\frac{m_e}{M_0}\mathbf{k}',c,-}(\mathbf{G}') C_{\mathbf{q}'-\frac{m_h}{M_0}\mathbf{k}',v,-}^*(\mathbf{G}' + \Delta\mathbf{G}') \\ &\quad \times \int d\mathbf{r}_e d\mathbf{r}_h V(\mathbf{R}, \mathbf{r}_{eh}) e^{i(\Delta\mathbf{G}-\mathbf{k})\cdot\mathbf{r}_e - i(\Delta\mathbf{G}'-\mathbf{k}')\cdot\mathbf{r}_h}. \end{aligned} \quad (\text{A4})$$

Note that $e^{i(\Delta\mathbf{G}-\mathbf{k})\cdot\mathbf{r}_c-i(\Delta\mathbf{G}'-\mathbf{k}')\cdot\mathbf{r}_h} = e^{i\frac{m_h}{M_0}(\Delta\mathbf{G}-\mathbf{k})+\frac{m_e}{M_0}(\Delta\mathbf{G}'-\mathbf{k}')\cdot\mathbf{r}_{ch}} e^{i(\Delta\mathbf{G}-\mathbf{k}-\Delta\mathbf{G}'+\mathbf{k}')\cdot\mathbf{R}}$. Since $V(\mathbf{R}, \mathbf{r}_{ch})$ varies very slowly with \mathbf{R} , $\int d\mathbf{R}V(\mathbf{R}, \mathbf{r}_{ch})e^{i(\Delta\mathbf{G}-\mathbf{k}-\Delta\mathbf{G}'+\mathbf{k}')\cdot\mathbf{R}} = \delta_{\Delta\mathbf{G}, \Delta\mathbf{G}'} \int d\mathbf{R}V(\mathbf{R}, \mathbf{r}_{ch})e^{-i(\mathbf{k}-\mathbf{k}')\cdot\mathbf{R}}$. So

$$\begin{aligned} J_{+-}(\mathbf{q}, \mathbf{q}', \mathbf{k}, \mathbf{k}') &= \sum_{\mathbf{G}, \mathbf{G}', \Delta\mathbf{G}} C_{\mathbf{q}+\frac{m_e}{M_0}\mathbf{k}, \mathbf{c}, +}^* (\mathbf{G}) C_{\mathbf{q}-\frac{m_h}{M_0}\mathbf{k}, \mathbf{v}, +} (\mathbf{G} + \Delta\mathbf{G}) C_{\mathbf{q}'+\frac{m_e}{M_0}\mathbf{k}', \mathbf{c}, -} (\mathbf{G}') C_{\mathbf{q}'-\frac{m_h}{M_0}\mathbf{k}', \mathbf{v}, -}^* (\mathbf{G}' + \Delta\mathbf{G}) \\ &\times \int d\mathbf{R} d\mathbf{r}_{ch} V(\mathbf{R}, \mathbf{r}_{ch}) e^{-i(\mathbf{k}-\mathbf{k}')\cdot\mathbf{R}} e^{i(\Delta\mathbf{G}-\frac{m_h}{M_0}\mathbf{k}-\frac{m_e}{M_0}\mathbf{k}')\cdot\mathbf{r}_{ch}} \\ &= J_{+-}^{\text{LR}}(\mathbf{q}, \mathbf{q}', \mathbf{k}, \mathbf{k}') + J_{+-}^{\text{SR}}(\mathbf{q}, \mathbf{q}', \mathbf{k}, \mathbf{k}'). \end{aligned} \quad (\text{A5})$$

Here the short-range part J_{+-}^{SR} can be ignored as it is much smaller than J_{+-}^{LR} . The long-range part is

$$J_{+-}^{\text{LR}}(\mathbf{q}, \mathbf{q}', \mathbf{k}, \mathbf{k}') = \frac{1}{A} \langle u_{\mathbf{q}+\frac{m_e}{M_0}\mathbf{k}, \mathbf{c}, +} | u_{\mathbf{q}-\frac{m_h}{M_0}\mathbf{k}, \mathbf{v}, +} \rangle \langle u_{\mathbf{q}'-\frac{m_h}{M_0}\mathbf{k}', \mathbf{v}, -} | u_{\mathbf{q}'+\frac{m_e}{M_0}\mathbf{k}', \mathbf{c}, -} \rangle V\left(\mathbf{k}-\mathbf{k}', \frac{m_h}{M_0}\mathbf{k} + \frac{m_e}{M_0}\mathbf{k}'\right), \quad (\text{A6})$$

and $V(\mathbf{Q}, \mathbf{q}) \equiv \int d\mathbf{r}_{ch} d\mathbf{R} e^{-i\mathbf{q}\cdot\mathbf{r}_{ch}} e^{-i\mathbf{Q}\cdot\mathbf{R}} V(\mathbf{R}, \mathbf{r}_{ch})$. We use the $\mathbf{k} \cdot \mathbf{p}$ expansion to evaluate the matrix element (and $m_e = m_h = m$),

$$\begin{aligned} \langle u_{\mathbf{q}+\frac{\mathbf{k}}{2}, \mathbf{c}, \tau} \rangle &= \langle u_{\mathbf{q}, \mathbf{c}, \tau} \rangle + \frac{\hbar}{2m} \mathbf{k} \cdot \sum_{n \neq \mathbf{c}} \frac{\langle u_{\mathbf{q}, n, \tau} | \hat{\mathbf{p}} | u_{\mathbf{q}, \mathbf{c}, \tau} \rangle}{E_{\mathbf{q}, \mathbf{c}, \tau} - E_{\mathbf{q}, n, \tau}} | u_{\mathbf{q}, n, \tau} \rangle + O(k^2) \\ \langle u_{\mathbf{q}-\frac{\mathbf{k}}{2}, \mathbf{v}, \tau} \rangle &= \langle u_{\mathbf{q}, \mathbf{v}, \tau} \rangle + \frac{\hbar}{2m} \mathbf{k} \cdot \sum_{n \neq \mathbf{v}} \frac{\langle u_{\mathbf{q}, n, \tau} | \hat{\mathbf{p}} | u_{\mathbf{q}, \mathbf{v}, \tau} \rangle}{E_{\mathbf{q}, n, \tau} - E_{\mathbf{q}, \mathbf{v}, \tau}} | u_{\mathbf{q}, n, \tau} \rangle + O(k^2). \end{aligned} \quad (\text{A7})$$

Then $\langle u_{\mathbf{q}+\frac{\mathbf{k}}{2}, \mathbf{c}, \tau} | u_{\mathbf{q}-\frac{\mathbf{k}}{2}, \mathbf{v}, \tau} \rangle = \frac{\hbar}{m} \mathbf{k} \cdot \frac{\langle u_{\mathbf{q}, \mathbf{c}, \tau} | \hat{\mathbf{p}} | u_{\mathbf{q}, \mathbf{v}, \tau} \rangle}{E_{\mathbf{q}, \mathbf{c}, \tau} - E_{\mathbf{q}, \mathbf{v}, \tau}} + O(k^2)$. We focus on the bright exciton within and near the light cone; thus, we need to keep only the leading term in \mathbf{k} . The optical dipole matrix element is $\mathbf{d}_{\mathbf{c}, \mathbf{v}, \tau} \equiv \frac{i\hbar}{m} \frac{\langle u_{\mathbf{q}, \mathbf{c}, \tau} | \hat{\mathbf{p}} | u_{\mathbf{q}, \mathbf{v}, \tau} \rangle}{E_{\mathbf{q}, \mathbf{c}, \tau} - E_{\mathbf{q}, \mathbf{v}, \tau}}$. So the intervalley matrix element is

$$J_{+-}(\mathbf{k}, \mathbf{k}') = (\mathbf{k} \cdot \mathbf{d}_{\mathbf{X}, +}) (\mathbf{k}' \cdot \mathbf{d}_{\mathbf{X}, -}^*) V\left(\mathbf{k}-\mathbf{k}', \frac{m_h}{M_0}\mathbf{k} + \frac{m_e}{M_0}\mathbf{k}'\right), \quad (\text{A8})$$

where the exciton transition dipole is $\mathbf{d}_{\mathbf{X}, +} = \mathbf{d}_{\mathbf{X}, -}^* = \frac{1}{\sqrt{A}} \sum_{\mathbf{q}} \Phi(\mathbf{q}) \mathbf{d}_{\mathbf{c}, \mathbf{v}, \mathbf{q}, +}$. Similarly, we can get the intervalley and intravalley matrix element as

$$J_{\tau, \tau'}(\mathbf{k}, \mathbf{k}') = (\mathbf{k} \cdot \mathbf{d}_{\mathbf{X}, \tau}) (\mathbf{k}' \cdot \mathbf{d}_{\mathbf{X}, \tau'}^*) V\left(\mathbf{k}-\mathbf{k}', \frac{m_h}{M_0}\mathbf{k} + \frac{m_e}{M_0}\mathbf{k}'\right). \quad (\text{A9})$$

APPENDIX B: PATTERNED DIELECTRIC SUPERLATTICE

The local dielectric constant $\varepsilon(\mathbf{R})$ [in Eq. (6)] changes smoothly at the lateral interfaces in the length scale $\Delta = 10$ nm. We transfer the spatial distribution $\varepsilon(\mathbf{R})$ to momentum space using the Fourier transform $\varepsilon(\mathbf{R})^{-1} = \varepsilon_0^{-1} \sum_{\mathbf{g}_n} \alpha(\mathbf{g}_n) e^{i\mathbf{g}_n \cdot \mathbf{r}}$. Here the wave vector $\mathbf{g}_n = (\frac{2\pi}{a_1+a_2}n, 0)$, and the corresponding coefficient

$$\alpha(\mathbf{g}_n) = \begin{cases} \frac{\xi_\varepsilon a_1 + a_2}{\xi_\varepsilon (a_1 + a_2)}, & n = 0, \\ \frac{2(1-\xi_\varepsilon)}{\xi_\varepsilon \Delta (a_1 + a_2)} \frac{\cos\left(\frac{a_1 + \Delta}{2} g_n\right) - \cos\left(\frac{a_1 - \Delta}{2} g_n\right)}{g_n^2}, & n \neq 0. \end{cases} \quad (\text{B1})$$

The quasi-1D pattern dielectric superlattice at $\xi_\varepsilon = 1.5$ with the smooth lateral interface Δ is shown in Fig. 5(a), while Fig. 5(b) presents the corresponding coefficients.

APPENDIX C: SCATTERING ANALYSIS IN A LATERAL DIELECTRIC INTERFACE

At a lateral dielectric interface, the Hamiltonian of an exciton in each region is Eq. (10), where the eigenvalue is $E_L(\mathbf{k}) = \frac{\hbar^2}{2M_0} k^2 + \frac{2J_\eta}{k} \frac{k^2}{k+k_s}$ or $E_T(\mathbf{k}) = \frac{\hbar^2}{2M_0} k^2$, with eigenvector $\Psi_{L/T}(\mathbf{r}) = \frac{1}{\sqrt{2}} e^{i\mathbf{k}\cdot\mathbf{r}} \{1, \pm e^{2i\theta}\}^T$, and $J_\eta = \frac{\varepsilon_0}{2\varepsilon_\eta} J$. For the whole lateral dielectric interface, the valley-orbit coupling is coordinate dependent, $J(x)$, due to the form of the dielectric (6). $J(x)$ approaches two different constants, J_2 and J_1 , in two different regions. First, we consider the width of the transition region $\Delta = 0$ and $k_s = 0$. We assume the L branch incidence with incident angle θ_L shown in Fig. 6(b); the exciton is regarded as a quasiparticle with wave function

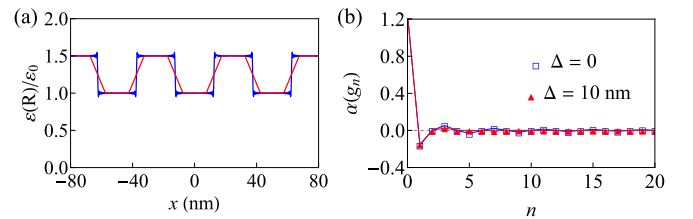


FIG. 5. (a) Numerical result of the periodic dielectric $\varepsilon(\mathbf{R})/\varepsilon_0$ as a function of the x axis. Parameters: $\xi_\varepsilon = 1.5$ and $\Delta = 0$ (blue line) and $\Delta = 10$ nm (red line). (b) The corresponding coefficients in the Fourier transform.

$$\Psi(\mathbf{r}) = \begin{cases} \frac{1}{\sqrt{2}} e^{ik_y y} \left[e^{ik_x L x} \begin{pmatrix} 1 \\ e^{2i\theta_L} \end{pmatrix} + r_L e^{-ik_x L x} \begin{pmatrix} 1 \\ e^{2i(\pi-\theta_L)} \end{pmatrix} + r_T e^{-ik_x T x} \begin{pmatrix} 1 \\ -e^{2i(\pi-\theta_T)} \end{pmatrix} \right], & x < 0, \\ \frac{1}{\sqrt{2}} e^{ik_y y} \left[t_L e^{iq_x L x} \begin{pmatrix} 1 \\ e^{2i\phi_L} \end{pmatrix} + t_T e^{iq_x T x} \begin{pmatrix} 1 \\ -e^{2i\phi_T} \end{pmatrix} \right], & x > 0, \end{cases} \quad (\text{C1})$$

where the kinetic momentum of the exciton satisfies

$$\begin{aligned} k_L &= \sqrt{\frac{4M_0^2 J_2^2}{\hbar^4 K^2} + \frac{2EM_0}{\hbar^2}} - \frac{2J_2 M_0}{\hbar^2 K}, \\ q_L &= \sqrt{\frac{4M_0^2 J_1^2}{\hbar^4 K^2} + \frac{2EM_0}{\hbar^2}} - \frac{2J_1 M_0}{\hbar^2 K}, \\ k_T &= q_T = \sqrt{\frac{2M_0 E}{\hbar^2}}, \quad k_y = k_L \sin \theta_L, \\ k_{x,L} &= k_L \cos \theta_L, \quad k_{x,T} = k_T \cos \theta_T, \quad q_{x,L} = q_L \cos \phi_L, \\ \theta_T &= \arcsin\left(\frac{k_L}{k_T} \sin \theta_L\right), \quad \phi_L = \arcsin\left(\frac{k_L}{q_L} \sin \theta_L\right), \\ \phi_T &= \arcsin\left(\frac{k_L}{q_T} \sin \theta_L\right). \end{aligned} \quad (\text{C2})$$

The boundary conditions at the interface point x_0 (i.e., $x_0 = 0$)

$$\begin{aligned} \hat{\beta}(J_2, k_{x,L}) \sqrt{\frac{J_2}{k_L}} \Psi(\mathbf{r}) \Big|_{x=x_0^-} &= \hat{\beta}(J_1, q_{x,L}) \sqrt{\frac{J_1}{q_L}} \Psi(\mathbf{r}) \Big|_{x=x_0^+}, \\ \sqrt{\frac{J_2}{k_L}} \Psi(x_0^-) &= \sqrt{\frac{J_1}{q_L}} \Psi(x_0^+), \end{aligned} \quad (\text{C3})$$

where the operator $\hat{\beta}$ in real space has

$$\hat{\beta}(J_\eta, k) = \begin{pmatrix} -\left(\frac{\hbar^2 k}{2M_0 J_\eta} + \frac{1}{K}\right) \frac{\partial}{\partial x} & -\frac{1}{K} \left(\frac{\partial}{\partial x} + 2k_y\right) \\ -\frac{1}{K} \left(\frac{\partial}{\partial x} - 2k_y\right) & -\left(\frac{\hbar^2 k}{2M_0 J_\eta} + \frac{1}{K}\right) \frac{\partial}{\partial x} \end{pmatrix}. \quad (\text{C4})$$

Combining the boundary condition (C3) with wave function (C1), the amplitude $\{r_L, r_T, t_L, t_T\}$ and reflection and transmission coefficients $R_{\chi \rightarrow \chi'}$ and $T_{\chi \rightarrow \chi'}$ are calculated.

Based on the conservation of spin in the scattering process, the numerical results of both the L and T branch incidences

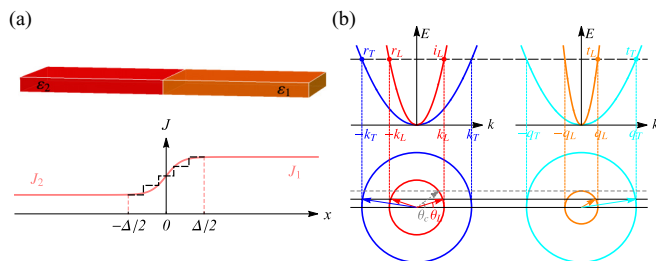


FIG. 6. (a) Scheme of the 1D patterned superlattice substrate, which provides the spatially modulating strength of the valley-orbit coupling $J(x)$. $J(x)$ approaches two different constants, J_2 and J_1 , in two different regions. A Δ -width transitional region occurs at the interface. (b) Schematic energy dispersion of the exciton at a lateral dielectric interface. Transmission and reflection coefficients at the L branch incidence are denoted.

are understood through the pseudospin texture analysis. The projection of a reflected or transmitted wave's pseudospin to incident wave's pseudospin $P_{r/t,\chi \rightarrow \chi'} = |\langle \chi_i | \chi'_{r/t} \rangle|^2 \cdot \chi_\mu$ is the valley pseudospin part of the exciton wave function, where $\mu \in \{i, r, t\}$ stands for the incident, reflected, or transmitted wave, respectively. Figures 7(c) and 7(d) show the pseudospin projection as a function of the incident angle. At the normal incidence of the L branch exciton $\theta_L = 0$ in Fig. 7(c), the pseudospins of the incident exciton and the intrabranch scattering exciton point in the same direction, i.e., $P_{r,L \rightarrow L} = P_{t,L \rightarrow L} = 1$. But they point in opposite directions for the interbranch scattering ($P_{r,L \rightarrow T} = P_{t,L \rightarrow T} = 0$). This leads to the fact that the intrabranch scattering occupies the total output,

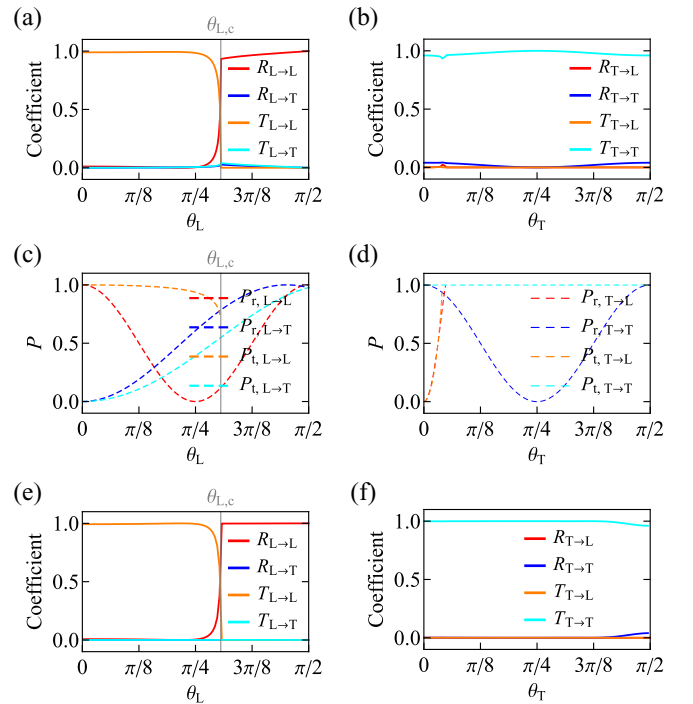


FIG. 7. Numerical results of scattering at a lateral interface where the two adjacent segments have distinct dielectric constants. Here the L branch transmission and reflection coefficients are denoted by $T_{\chi \rightarrow L}$ (orange solid lines) and $R_{\chi \rightarrow L}$ (red solid lines), respectively, along with the T branch transmission coefficient $T_{\chi \rightarrow T}$ (cyan solid lines) and reflection $R_{\chi \rightarrow T}$ (blue solid lines). The branch index of the incident exciton is $\chi = L, T$. The pseudospin projection is marked by a corresponding dashed line. In the sharp interface case, (a) the transmission and reflection coefficients and (c) pseudospin projection $P_{\mu,\sigma}$ as functions of the incident angle θ_L at the L branch incidence. (b) and (d) The T branch incidence with incident angle θ_T . (e) and (f) The scattering result with a nonzero transition region at the interface. Parameters: $E = 5$ meV, $J = 2$ eV, $k_s = 0$, $\epsilon_\xi = 1.25$, and transitional region $\Delta = 20$ nm.

while the interbranch scattering is quite weak. When θ_L surpasses the critical angle $\theta_{L,c}$, the oscillating transmitted wave of the L branch vanishes, and total internal reflection emerges. The numerical result for the T branch incidence is shown in Fig. 7(d). When the incident angle θ_T changes from 0 to $\pi/2$, the pseudospin of the incident exciton and the T branch transmitted exciton always point in the same direction, i.e., $P_{T \rightarrow T} = 1$. This indicates that the intrabranched transmission coefficient $T_{T \rightarrow T}$ plays the dominant role in the outputs.

We consider a Δ -width transitional region where the local dielectric constant changes continuously from the value of the left region to that of the right region. In the scattering calculation, this transitional region is divided into n equal pieces of small step functions, in which the wave functions are matched with the boundary conditions. The excitons feel the dielectric constant $\varepsilon_i = [i\varepsilon_1 + (n-i)\varepsilon_2]/n$ at the i th piece shown in Fig. 6(a). The valley-orbit coupling amplitude has $J_i = \frac{\varepsilon_0}{2\varepsilon_i} J$. For each region, the two-component wave function of the exciton $\Psi_i(\mathbf{r}) = \{\psi_{1,i}(\mathbf{r}), \psi_{2,i}(\mathbf{r})\}^T$,

$$\begin{aligned} \psi_{1,i}(\mathbf{r}) &= \frac{1}{\sqrt{2}} e^{ik_y y} (a_i e^{ik_{x,L,i} x} + b_i e^{-ik_{x,L,i} x} + c_i e^{ik_{x,T} x} + d_i e^{-ik_{x,T} x}), \\ \psi_{2,i}(\mathbf{r}) &= \frac{1}{\sqrt{2}} e^{ik_y y} (a_i e^{ik_{x,L,i} x + 2i\theta_{L,i}} + b_i e^{-ik_{x,L,i} x - 2i\theta_{L,i}} \\ &\quad - c_i e^{ik_{x,T} x + 2i\theta_T} - d_i e^{-ik_{x,T} x - 2i\theta_T}), \end{aligned} \quad (C5)$$

where the kinetic momentum

$$\begin{aligned} k_{L,i} &= \sqrt{\frac{4M_0^2 J_i^2}{\hbar^4 K^2} + \frac{2EM_0}{\hbar^2} - \frac{2J_i M_0}{\hbar^2 K}}, \quad k_T = \sqrt{\frac{2M_0 E}{\hbar^2}}, \\ k_{x,L,i} &= k_{L,i} \cos \theta_{L,i}, \quad \theta_{L,i} = \arcsin\left(\frac{k_{L,0}}{k_{L,i}} \sin \theta_{L,0}\right), \\ k_{x,T} &= k_T \cos \theta_T, \quad \theta_T = \arcsin\left(\frac{k_{L,0}}{k_T} \sin \theta_{L,0}\right), \end{aligned} \quad (C6)$$

where the incident angle $\theta_{L,0} = \theta_L$, $a_0 = 1$, and $c_0 = b_n = d_n = 0$. The transmission and reflection coefficients are determined via the boundary conditions at all the joint points. The numerical scattering result of the L branch incident with the incident angle θ_L is shown in Fig. 7(e). The dominant role of the intrabranched scattering output ($R_{L \rightarrow L} + T_{L \rightarrow L}$) is enhanced. At the T branch incidence in Fig. 7(f), T_T approaches 1, while R_T is evidently suppressed. This illustrates that the dielectric heterostructure seems to be nearly transparent for the propagating exciton of the T branch.

APPENDIX D: ROBUSTNESS OF THE 1D FEATURES OF THE EXCITON'S WAVE FUNCTION

Based on the expression for the exchange Hamiltonian, Eq. (9), the different forms of the Coulomb interactions do not change the previous main results. Considering a dielectric superlattice $\varepsilon(\mathbf{R})$ in Eq. (6) with $\Delta = 10$ nm and $\xi_\varepsilon = 1.5$,

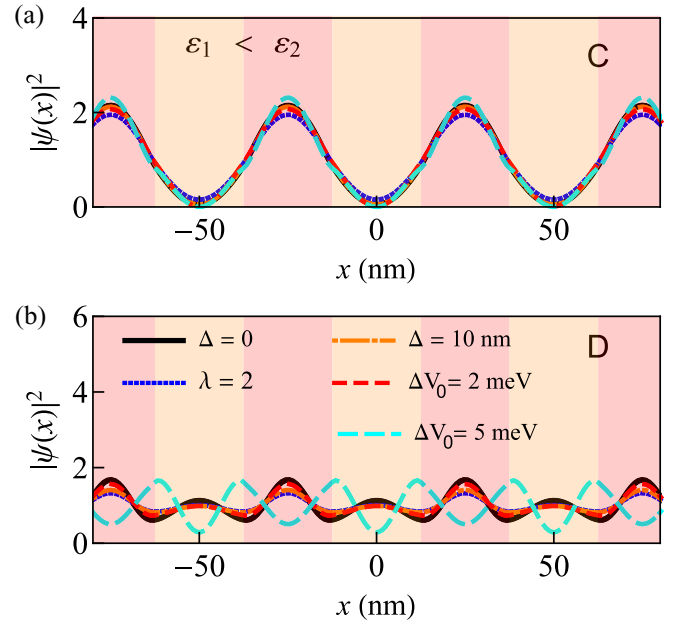


FIG. 8. Probability distribution of the L branch exciton with a 1D periodic dielectric superlattice at momentum points C and D [see Fig. 3(a)]. The alternating colored regions denote the different dielectric constants ε_1 and ε_2 . The black solid line stands for the $\Delta = 0$ case. The orange dot-dashed line stands for the $\Delta = 10$ nm case. The blue dotted line is the screening wave vector with the $\lambda = 2$ case. The red (cyan) dashed line is the case with energy modulation $\Delta V_0 = 2$ meV (5 meV).

the exciton densities of the L branch at the C and D points [the momentum points marked in Fig. 3(a)] are denoted by the gray dashed lines in Fig. 8. Compared to the $\Delta = 0$ case (black solid lines), the gray dashed lines illustrate quantitatively that the main results are independent of the Coulomb interactions. Similarly, the parameter λ of the screening wave vector $k_0(\mathbf{g}) = \lambda \mathbf{g}$ in Eq. (9) is changed (for instance, $\lambda = 2$). The results are denoted by the blue dotted line in Fig. 8(b), and the density distribution is almost unchanged.

Due to the cancellation of the changes to the exciton binding energy and electronic band gap, we have ignored the change in the exciton energy when the dielectric environment is modulated. In realistic systems, both the \mathbf{K} and $-\mathbf{K}$ valley excitons feel a residual small energy modulation described by $\Delta \hat{H} = \sum_{\mathbf{k}, \mathbf{g}} \Delta V(\mathbf{g}) (\hat{B}_{\mathbf{k},+}^\dagger \hat{B}_{\mathbf{k}+\mathbf{g},+} + \hat{B}_{\mathbf{k},-}^\dagger \hat{B}_{\mathbf{k}+\mathbf{g},-})$, where $\Delta V(\mathbf{g})$ is the Fourier coefficient of the modulated potential in real space $\Delta V(\mathbf{R})$. ΔV_0 denotes the different $\Delta V(\mathbf{R})$ in different dielectric constant regions. We find that the density distribution (marked by the red dashed line in Fig. 8) is almost unchanged when the potential is modulated slightly, $\Delta V_0 = 2$ meV. But at $\Delta V_0 = 5$ meV (cyan dashed line), such a significant potential modulation causes the mode which concentrates in low- ε regions to perform at higher energy than the mode where high ε is dominant.

[1] Q. H. Wang, K. Kalantar-Zadeh, A. Kis, J. N. Coleman, and M. S. Strano, *Nat. Nanotechnol.* **7**, 699 (2012).

[2] X. Xu, W. Yao, D. Xiao, and T. F. Heinz, *Nat. Phys.* **10**, 343 (2014).

- [3] G.-B. Liu, D. Xiao, Y. Yao, X. Xu, and W. Yao, *Chem. Soc. Rev.* **44**, 2643 (2015).
- [4] K. F. Mak, C. Lee, J. Hone, J. Shan, and T. F. Heinz, *Phys. Rev. Lett.* **105**, 136805 (2010).
- [5] A. Splendiani, L. Sun, Y. Zhang, T. Li, J. Kim, C.-Y. Chim, G. Galli, and F. Wang, *Nano Lett.* **10**, 1271 (2010).
- [6] A. M. Jones, H. Yu, N. J. Ghimire, S. Wu, G. Aivazian, J. S. Ross, B. Zhao, J. Yan, D. G. Mandrus, D. Xiao, W. Yao, and X. Xu, *Nat. Nanotechnol.* **8**, 634 (2013).
- [7] J. S. Ross, S. Wu, H. Yu, N. J. Ghimire, A. M. Jones, G. Aivazian, J. Yan, D. G. Mandrus, D. Xiao, W. Yao *et al.*, *Nat. Commun.* **4**, 1474 (2013).
- [8] K. F. Mak, K. He, C. Lee, G. H. Lee, J. Hone, T. F. Heinz, and J. Shan, *Nat. Mater.* **12**, 207 (2013).
- [9] D. Y. Qiu, F. H. da Jornada, and S. G. Louie, *Phys. Rev. Lett.* **111**, 216805 (2013).
- [10] D. Xiao, G.-B. Liu, W. Feng, X. Xu, and W. Yao, *Phys. Rev. Lett.* **108**, 196802 (2012).
- [11] W. Yao, D. Xiao, and Q. Niu, *Phys. Rev. B* **77**, 235406 (2008).
- [12] H. Yu, G.-B. Liu, P. Gong, X. Xu, and W. Yao, *Nat. Commun.* **5**, 3876 (2014).
- [13] H. Yu, X. Cui, X. Xu, and W. Yao, *Natl. Sci. Rev.* **2**, 57 (2015).
- [14] D. Y. Qiu, T. Cao, and S. G. Louie, *Phys. Rev. Lett.* **115**, 176801 (2015).
- [15] F. Wu, F. Qu, and A. H. MacDonald, *Phys. Rev. B* **91**, 075310 (2015).
- [16] M. Katsnelson, K. Novoselov, and A. Geim, *Nat. Phys.* **2**, 620 (2006).
- [17] V. V. Cheianov and V. I. Fal'ko, *Phys. Rev. B* **74**, 041403(R) (2006).
- [18] V. V. Cheianov, V. Fal'ko, and B. Altshuler, *Science* **315**, 1252 (2007).
- [19] A. I. Prazdnichnykh, M. M. Glazov, L. Ren, C. Robert, B. Urbaszek, and X. Marie, *Phys. Rev. B* **103**, 085302 (2021).
- [20] M. M. Ugeda, A. J. Bradley, S.-F. Shi, H. Felipe, Y. Zhang, D. Y. Qiu, W. Ruan, S.-K. Mo, Z. Hussain, Z.-X. Shen *et al.*, *Nat. Mater.* **13**, 1091 (2014).
- [21] A. J. Bradley, M. M. Ugeda, F. H. da Jornada, D. Y. Qiu, W. Ruan, Y. Zhang, S. Wickenburg, A. Riss, J. Lu, S.-K. Mo *et al.*, *Nano Lett.* **15**, 2594 (2015).
- [22] S. Latini, T. Olsen, and K. S. Thygesen, *Phys. Rev. B* **92**, 245123 (2015).
- [23] A. V. Stier, N. P. Wilson, G. Clark, X. Xu, and S. A. Crooker, *Nano Lett.* **16**, 7054 (2016).
- [24] J. Ryou, Y.-S. Kim, K. Santosh, and K. Cho, *Sci. Rep.* **6**, 29184 (2016).
- [25] A. Raja, A. Chaves, J. Yu, G. Arefe, H. M. Hill, A. F. Rigosi, T. C. Berkelbach, P. Nagler, C. Schüller, T. Korn *et al.*, *Nat. Commun.* **8**, 15251 (2017).
- [26] Y. Cho and T. C. Berkelbach, *Phys. Rev. B* **97**, 041409(R) (2018).
- [27] M. I. B. Utama, H. Kleemann, W. Zhao, C. S. Ong, H. Felipe, D. Y. Qiu, H. Cai, H. Li, R. Kou, S. Zhao *et al.*, *Nat. Electron.* **2**, 60 (2019).
- [28] S. Gao, Y. Liang, C. D. Spataru, and L. Yang, *Nano Lett.* **16**, 5568 (2016).
- [29] A. Raja, L. Waldecker, J. Zipfel, Y. Cho, S. Brem, J. D. Ziegler, M. Kulig, T. Taniguchi, K. Watanabe, E. Malic *et al.*, *Nat. Nanotechnol.* **14**, 832 (2019).
- [30] Y. Xu, S. Liu, D. A. Rhodes, K. Watanabe, T. Taniguchi, J. Hone, V. Elser, K. F. Mak, and J. Shan, *Nature (London)* **587**, 214 (2020).
- [31] Y. Lin, X. Ling, L. Yu, S. Huang, A. L. Hsu, Y.-H. Lee, J. Kong, M. S. Dresselhaus, and T. Palacios, *Nano Lett.* **14**, 5569 (2014).
- [32] C. Forsythe, X. Zhou, K. Watanabe, T. Taniguchi, A. Pasupathy, P. Moon, M. Koshino, P. Kim, and C. R. Dean, *Nat. Nanotechnol.* **13**, 566 (2018).
- [33] Y. Li, S. Dietrich, C. Forsythe, T. Taniguchi, K. Watanabe, P. Moon, and C. R. Dean, *Nat. Nanotechnol.* **16**, 525 (2021).
- [34] Y. Xu, C. Horn, J. Zhu, Y. Tang, L. Ma, L. Li, S. Liu, K. Watanabe, T. Taniguchi, J. C. Hone *et al.*, *Nat. Mater.* **20**, 645 (2021).
- [35] A. Chernikov, T. C. Berkelbach, H. M. Hill, A. Rigosi, Y. Li, O. B. Aslan, D. R. Reichman, M. S. Hybertsen, and T. F. Heinz, *Phys. Rev. Lett.* **113**, 076802 (2014).
- [36] T. Matsuyama, C.-M. Hu, D. Grundler, G. Meier, and U. Merkt, *Phys. Rev. B* **65**, 155322 (2002).